Applied Catalysis B: Environmental 204 (2017) 584–592

Contents lists available at ScienceDirect

Applied Catalysis B: Environmental

journal homepage: www.elsevier.com/locate/apcatb

A new strategy for utilization of NIR from solar energy—Promotion effect generated from photothermal effect of $Fe_3O_4@SiO_2$ for photocatalytic oxidation of NO

Jing Hu [a,b], Haiqiang Wang [a,b,*], Fan Dong [c], Zhongbiao Wu [a,b,*]

[a] Key Laboratory of Environment Remediation and Ecological Health, Ministry of Education, College of Environmental & Resources Science, Zhejiang University, Hangzhou 310058, PR China
[b] Zhejiang Provincial Engineering Research Center of Industrial Boiler & Furnace Flue Gas Pollution Control, Hangzhou 310027, PR China
[c] Chongqing Key Laboratory of Catalysis and Functional Organic Molecules, College of Environment and Resources, Chongqing Technology and Business University, 400067 Chongqing, PR China

ARTICLE INFO

Article history:
Received 19 September 2016
Received in revised form
17 November 2016
Accepted 3 December 2016
Available online 6 December 2016

Keywords:
Photothermal effect
$Fe_3O_4@SiO_2$
Photocatalytic oxidation
NO

ABSTRACT

Photothermal effect was for the first time utilized to capture the energy from infrared light and to promote the photocatalytic oxidation activity of NO by a simply mechanical mixing of traditional photocatalysts and core-shell structured $Fe_3O_4@SiO_2$. $Fe_3O_4@SiO_2$ absorbed the infrared light, transferred it into thermal energy based on photothermal effect, which then accelerated the NO photocatalytic activity of traditional photocatalysts. This promotion effect led by the addition of $Fe_3O_4@SiO_2$ was confirmed by several classical photocatalysts such as TiO_2, g-C_3N_4, BiOI and CeO_2. To quantitatively characterize the photothermal effect, thermo images were taken with a thermo imager to obtain the average temperature rise of samples under the illumination of simulated solar light. Specially, P25/$Fe_3O_4@SiO_2$ was studied in depth for illustration of the promotion mechanism. Experimental results showed that with the contribution of SiO_2 shell, the photocorrosion of Fe_3O_4 didn't occur during photocatalytic oxidation process and the photothermal effect of Fe_3O_4 was maintained. The quantity of $Fe_3O_4@SiO_2$ was a vital factor for promotion of photocatalytic activity and the optimum mass ratio of P25 and $Fe_3O_4@SiO_2$ was 3–1. After 120 min of illumination, the temperature of optimum P25/$Fe_3O_4@SiO_2$ rose to 57.4 °C from 25 °C and its NO conversion capability showed an enhancement of 38.9% with the comparison to pure P25. The experimental results confirmed that the rise of temperature was attributed to the photothermal effect and its contribution was the same as the directly heating of photocatalysts. Furthermore, the enhancement of NO conversion capability around 30–40% was observed for the $Fe_3O_4@SiO_2$ mixed anatase TiO_2, g-C_3N_4, ZnO, BiOI and CeO_2. In sum, we developed a new strategy for utilization of NIR light of solar energy to facilitate the photocatalytic reactions.

1. Introduction

Efficient harvesting of solar energy is always a big challenge and a worldwide target for human being. For this challenge, heterogeneous photocatalysis using nano-scale semiconductor materials has attracted enormous interests. TiO_2 was a famous nanomaterial among these semiconductors and has been widely used as photocatalyst. However, TiO_2 has a large bandgap of ~3.2 eV [1,2] (for anatase phase) and requires UV light (<380 nm) to be activated, while the percentage of UV light in solar energy was only ~5% and more than 90% of overall solar spectrum consisted of visible light (about ~49%) and near infrared (NIR) light (about ~46%). In the past ten years, researchers paid lots of attentions to the utilization of visible light energy and they gained remarkable progress. Photocatalysts with narrow bandgap and broad absorption spectrum were developed or discovered. Besides the metal or non-metal modified TiO_2 [3], a lot of new photocatalysts such as g-C_3N_4 [4], $(BiO)_2CO_3$

* Corresponding authors at: Key Laboratory of Environment Remediation and Ecological Health, Ministry of Education, College of Environmental & Resources Science, Zhejiang University, Hangzhou 310058, PR China.
E-mail addresses: haiqiangwang@zju.edu.cn, wanghaiqiang2008@126.com (H. Wang), zbwu@zju.edu.cn (Z. Wu).

http://dx.doi.org/10.1016/j.apcatb.2016.12.009
0926-3373/

[5], BiOX [6], etc. appeared. However, the utilization of NIR light which accounts for about 44% in the solar spectrum [7] is seldom reported [8].

The photothermal effect of nanoparticles on tumor photothermal ablation therapy (PTA) has been a research focus currently [9,10]. With the irradiation of NIR, the tumor cells containing proper photothermal agents were killed due to high temperature resulted from photothermal effect. Photothermal agents such as organic compounds (indocyanine green [11], polyaniline nanoparticles [12], etc.), noble metal nanomaterials (Au [13], Ag [14] and Pd [15], etc.), carbon-based materials (carbon nanotubes [16], graphene [9,17,18], etc.) and transition metal nanoparticles (Fe_3O_4 [19–21], Cu_3BiS_3 [22], Cu_9S_5 [23] and Ti_8O_{15} [1], etc.) have been studied. Noble metal nanoparticles (NPs) of Au, Ag, and Pd that support LSPR in the visible spectrum were the most studied plasmonic NPs, but they were expensive for application. Compared to noble metal NPs, transition metal NPs-Fe_3O_4 showed a list of desirable properties for efficient and stable photothermal reactions: (i) a substantial photon absorption cross-section, (ii) strong intraparticle bonds, (iii) strong bonds to any surfactants, and (iV)environmental friendly and economical [24]; that's why it attracted researchers' attention in photothermal applications.

Nowadays, the studies on graphene-based nanocomposites, $NaYF_4$:Yb,Tm@TiO_2 and Ti@TiO_2 for photocatalysis inspired us and attract our interesting for the utilization of NIR light. Zhixing Gan et al. [25] reported that the photothermal effect of graphene-based nanocomposites could play an important role in enhancing photocatalytic performance. Yanna Tang et al. had synthesized a core-shell $NaYF_4$:Yb,Tm@TiO_2 by using a solvothermal method to response to NIR. It was found that the upconversion luminescence $NaYF_4$:Yb, Tm core could absorb NIR light and give out UV light which could be absorbed by the anatase TiO_2 shell [26]. Also, a stable core-shell Ti@TiO_2 with NIR response was reported. The photocatalyst could response from UV to NIR light region and exhibited photothermal effect as a result of Ti core [27]. These works pointed out a new path for the utilization of NIR light energy, but currently there was very few studies focused on Fe_3O_4 and gas-solid phase photocatalytic reaction.

As one of the major air pollutants, NO is difficult to be removed by the widely used wet scrubbing methods because NO is nearly insoluble in water [28]. At present, the most effective method of NO removal, selective catalytic reduction (SCR), is expensive and requires extreme conditions including high temperature and toxic ammonia. Therefore, photocatalytic oxidation of NO, in which NO is oxidized into soluble species at low temperature and without introduction of toxic ammonia, costs less and has good potential in industrial application [29]. Herein, for the first time, we selected Fe_3O_4 NPs as photothermal agent to improve utilization of NIR light from solar energy for photocatalytic oxidation of NO. We intended to take advantage of this energy to enhance NO conversion of photocatalysts. But we also concerned that Fe_3O_4 NPs would be oxidized while it exposed to photocatalyst due to the producted HNO_3. To prevent this oxidation, Fe_3O_4 NPs was coated with a passive material, such as SiO_2, to form a core-shell structured Fe_3O_4@SiO_2. Series of composed photocatalysts were synthesized by simply mixing traditional photocatalysts and core-shell structured Fe_3O_4@SiO_2 together mechanically, such as g-C_3N_4/Fe_3O_4@SiO_2, BiOI/Fe_3O_4@SiO_2, and CeO_2/Fe_3O_4@SiO_2. The physicochemical properties of prepared photocatalysts were studied and a new characterization method-thermo image was used to obtain the average surface temperature rise on the photocatalysts by photothermal effect (i.e. analyzing the photothermal effect quantitatively). The promotion effect caused by photothermal effect from NIR light in photocatalytic oxidation of NO was discussed and its promotion mechanism was proposed.

2. Experimental

2.1. Sample preparation

$FeCl_3{\cdot}6H_2O$, $NH_3{\cdot}H_2O$ solution (25%–28%) and PEG2000 were purchased from Sinopharm Chemical Reagent Co. Ltd., China. $FeSO_4{\cdot}7H_2O$ was purchased from Quzhou JuHua reagent Co., Ltd., China. P25 was purchased from Evonik Degussa, AG. TEOS was obtained from Aladdin Industrial Co., Shanghai, China.

2.1.1. Fe_3O_4 and Fe_3O_4@SiO_2

Fe_3O_4 was prepared using a coprecipitation method under an atmosphere of nitrogen as reported previously [20]. In a typical synthesis, $FeCl_3{\cdot}6H_2O$ (9.41 g) and $FeSO_4{\cdot}7H_2O$ were dissolved in 50 mL DI water by ultrasonic in a three-necked round-bottom flask with nitrogen bubbling. Under vigorous mechanical stirring, 50 mL PEG2000 solution (400 g/L) was added to the solution. When the solution was homogeneous blended, 70 mL $NH_3{\cdot}H_2O$ (8%) was introduced dropwise to the solution. After stirring for 1 h and left for another 1 h at 60 °C, the black precipitate was washed with ethanol and DI water for three times.

The as prepared Fe_3O_4 was coated with silica by the Stöber method whereas 0.4 g of Fe_3O_4 was thoroughly dispersed in 40 mL ethanol with sonication for 30 min, and then 2 mL of the ammonia solution was added into the solution. With mechanical stirring, 1.6 mL TEOS was added to the solution. After stirring for 3 h, the products were washed with ethanol and DI water for several times and finally dried at 60 °C in vacuum for 6 h.

2.1.2. Composed photocatalyst/Fe_3O_4@SiO_2(x:1)

Composed photocatalyst/Fe_3O_4@ SiO_2(x:1) was prepared by solid–solid mixing method. Base photocatalyst represents sample with photocatalytic capability for NO oxidation, that is P25, anatase TiO_2 (A-TiO_2), g-C_3N_4, ZnO, BiOI, or CeO_2. The x:1 stands for the mass ratio of base photocatalyst and Fe_3O_4@SiO_2. In particular, sample with optimum mass ratio is recorded as Base photocatalyst/Fe_3O_4@SiO_2.

A-TiO_2 [30], g-C_3N_4 [31], ZnO [32], BiOI [33] and CeO_2 [30] were prepared by the methods reported in References.

2.2. Characterization

X-ray diffraction (XRD, model D/max RA, Rigaku Co., Japan with Cu Kα radiation) was conducted to analyze the crystal phase and composition of the samples. X-ray photoelectron spectroscopy (XPS) measurements for analyzing the surface properties were performed using a Thermo ESCALAB 250 instrument equipped with Al Kα X-ray irradiation (1486.6 eV) at 150 W. The binding energy scale was corrected referenced to the C1s level at 285 eV. The morphology of the samples was obtained from scanning electron microscopy (SEM, FEI-quanta 200F, USA) and transmission electron microscope (TEM, H-600, Hitachi, Ltd., Japan). The specific surface areas were determined with a static adsorption instrument (JW-BK 132F, Beijing JWGB Sci & Tech Co., China) by the Brunauer–Emmett–Teller (BET) method. UV–vis-NIR spectra were obtained from a UV–vis-NIR spectrophotometer (SOLID3700, Shimadzu, Japan). Thermo images were taken with a thermo imager (Testo Co., Ltd., Testo 885) to perform quantitative analyses of photothermal effect of samples. A testo IR soft was used to obtain the average temperature distribution for every thermo image. Thermogravimetry (TG) was measured by a simultaneous thermal analyzer (STA 409 PC NETZSCH, Germany) at a heating rate of 10 °C/min in air flowing of 20 mL/min. Raman spectra were obtained from a SPEX-1403 laser Raman spectroscopy at room temperature. A 514.5 nm Ar-ion laser in a backscattering configuration was used to excite the crystals (Raman: Lab RAM-HR, SPEX-1403, France). In-

situ Fourier Transform Infrared Spectroscopy (in-situ FTIR) spectra were obtained from a Tensor 27 (Bruker, Germany).

2.3. Photocatalytic experiments

Photocatalytic experiments were carried out in a continuous flow rectangular reactor with controllable temperature. The stainless steel reactor consisting of 5 S-shaped channels (30 mm × 100 mm × 20 mm) was covered with quartz glass. A 500 W Xenon lamp (Shenzhen AHD Opto Technology Co. Ltd.) with adjustable voltage was placed above the reactor and the voltage was set to 7 V for every test. The photocatalysts were coated on five glass slide (28 mm × 95 mm) with a dip-coating method and 0.05 g photocatalyst was used for every slide. Photocatalysts were naturally dried before the experiment. 50 ppm of NO gas was obtained from an air cylinder, a N_2 cylinder (99.9%) and a NO cylinder (10,000 ppm, diluted by N_2). The relative humidity (RH) was regulated to 70% by passing the air stream through a humidification chamber and RH was monitored by a relative humidity analyzer (Testo Co., Ltd., Model 605-H1). The flow rate was controlled at 2 L/min and the residence time was 9 s. After thoroughly mixed in a gas blender, the streams got into the reactor. When the concentration of NO in inlet and outlet achieved equilibrium, the lamp was turned on and the photocatalytic reaction continued for 120 min. The concentration of NO and NO_2 was measured by a NO_x analyzer (Kane International Ltd., Model KM-9106). The NO conversion was calculated as *NO conversion* $(\%) = (1 - NO_{out}/NO_{in}) \times 100\%$, where NO_{out} and NO_{in} represented the concentration of NO in outlet and inlet separately. The NO_2 selectivity was calculated as NO_2 *selectivity* $(\%) = (NO_{2,out} - NO_{2,in})/(NO_{in} - NO_{out}) \times 100\%$, where $NO_{2,out}$ and $NO_{2,in}$ represented the concentration of NO_2 in outlet and inlet separately.

The reactor was controlled at 25 °C, 50 °C, 60 °C, 70 °C respectively to study the influence of temperature on photocatalytic activity of P25. Without specially illustration, photocatalytic experiments were conducted at 25 °C. In order to acquire the photocatalytic activity of photocatalysts free from infrared (P25-cut IR and $P25/Fe_3O_4@SiO_2$(3:1)-cut IR), an infrared cut-off filter (Rayan Technology Co. Ltd., Model SP730) was placed on the quarts of the reactor. Another optical filter (China Nantong yinxing Optical Products Co. Ltd., HWB 780) was used to obtain NIR and the photocatalytic activity under NIR was studied.

3. Results and discussion

3.1. Crystal phase analysis by XRD

Fig. 1 shows the XRD patterns of investigated samples. The XRD patterns of Fe_3O_4 indicated that the prepared Fe_3O_4 was with a highly crystalline cubic spinel structure (PDF no. 85-1436). The positions and intensities of reflection peaks of sample agreed well with Fe_3O_4 reported in previous study [34], and the core-shell structure of $Fe_3O_4@SiO_2$ didn't affect the phase structure of Fe_3O_4 after the coating of SiO_2. Characteristic peaks at 2θ = 30.38°, 35.34°, 43.38°, 53.88°, 57.36° and 62.94° which were respectively corresponded to lattice plane (220), (311), (400), (422), (511) and (440) of Fe_3O_4, were all observed on $Fe_3O_4@SiO_2$. After solid mixing of $Fe_3O_4@SiO_2$, the intensities of characteristic peaks for anatase and rutile of $P25/Fe_3O_4@SiO_2$ were slightly weaker compared to that of P25. The peaks at 25.05°(101), 37.96°(004), 38.75°(112), 48.05°(200), 54.08°(105), 55.22°(211), 62.80°(204), 70.46°(200) were corresponded to anatase phase (PDF no. 21-1272), the peaks at 27.62°(110), 36.20°(101), 62.80°(002), 69.14°(301) were corresponded to rutile phase (PDF no. 21-1276) and the peaks at 35.34° and 57.36° confirmed the existence of Fe_3O_4. Also, the XRD spectra of A $TiO_2/Fe_3O_4@SiO_2$, $g\text{-}C_3N_4/Fe_3O_4@SiO_2$, $ZnO/Fe_3O_4@SiO_2$, $BiOI/Fe_3O_4@SiO_2$, and $CeO_2/Fe_3O_4@$ SiO_2 were shown in Fig. S1. The existence of Fe_3O_4 and other photocatalysts were all confirmed and no other crystal phase was detected in the XRD spectra.

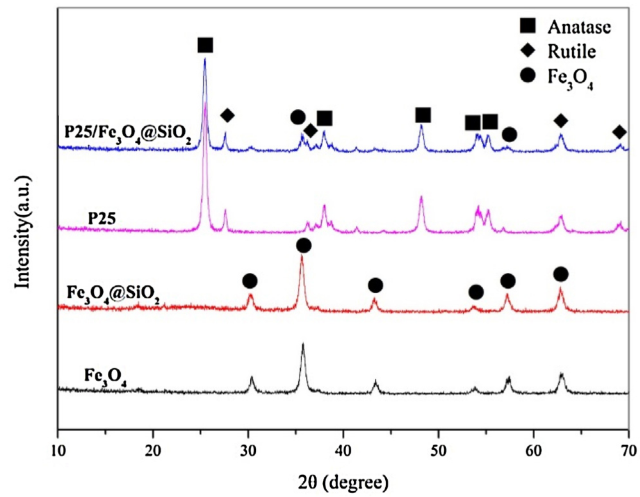

Fig. 1. XRD patterns of samples.

Table 1
The physical characteristics of prepared samples.

Sample	Surface area ($m^2 \cdot g^{-1}$)	Pore volume ($cm^3 \cdot g^{-1}$)	Pore size (nm)
P25	49.49	0.17	8.67
Fe_3O_4	59.54	0.33	15.62
$Fe_3O_4@SiO_2$	26.75	0.08	5.59
$P25/Fe_3O_4@SiO_2$	47.31	0.23	8.85

3.2. Morphology, pore structure and formation mechanism

The morphology, particles size and micro-structure of samples were shown in Fig. 2. The SEM image of Fe_3O_4 was shown in Fig. 2a. As depicted, uniform spherical Fe_3O_4 nanoparticles were synthesized and the average diameter of Fe_3O_4 NPs was around 22 nm. Fig. 2b shows the SEM image of $Fe_3O_4@SiO_2$. After the coating of SiO_2, all Fe_3O_4 NPs were coated by a uniform SiO_2 shell and the average diameter of $Fe_3O_4@SiO_2$ was enlarged to 30–40 nm. Fig. 2c shows the SEM image of $P25/Fe_3O_4@SiO_2$. TiO_2 NPs and $Fe_3O_4@SiO_2$ NPs were mixed uniformly and there was no evident difference compared to Fe_3O_4 NPs. The high resolution TEM image of prepared samples was also shown in Fig. 2. Fig. 2d shows the TEM image of Fe_3O_4 NPs. As shown in image, Fe_3O_4 was spherical structure and the average diameter was around 20–30 nm. With the coating of SiO_2, a core-shell structure of $Fe_3O_4@SiO_2$ was investigated in Fig. 2e. Obviously, the core-shell structure was composed of a Fe_3O_4 core (20–30 nm) and a SiO_2 shell (3–5 nm). TEM image of $P25/Fe_3O_4@$ SiO_2 was shown in Fig. 2f. It confirmed that TiO_2 NPs was uniformly mixed with $Fe_3O_4@SiO_2$ NPs.

Table 1 shows the specific surface area, pore volume and pore size for photocatalysts. After coating of SiO_2, the surface area of $Fe_3O_4@SiO_2$ decreased from 59.54 $m^2 \cdot g^{-1}$ of Fe_3O_4 to 26.75 $m^2 \cdot g^{-1}$. When P25 and $Fe_3O_4@SiO_2$ were mixed, the physical characteristics of $P25/Fe_3O_4@SiO_2$ were similar to those of P25 because of the low mixture percentage of $Fe_3O_4@SiO_2$.

After analyzing TEM images and physical characteristics of the samples, the formation process of core-shell structured $P25/Fe_3O_4@SiO_2$ was proposed and shown in Fig. 3.

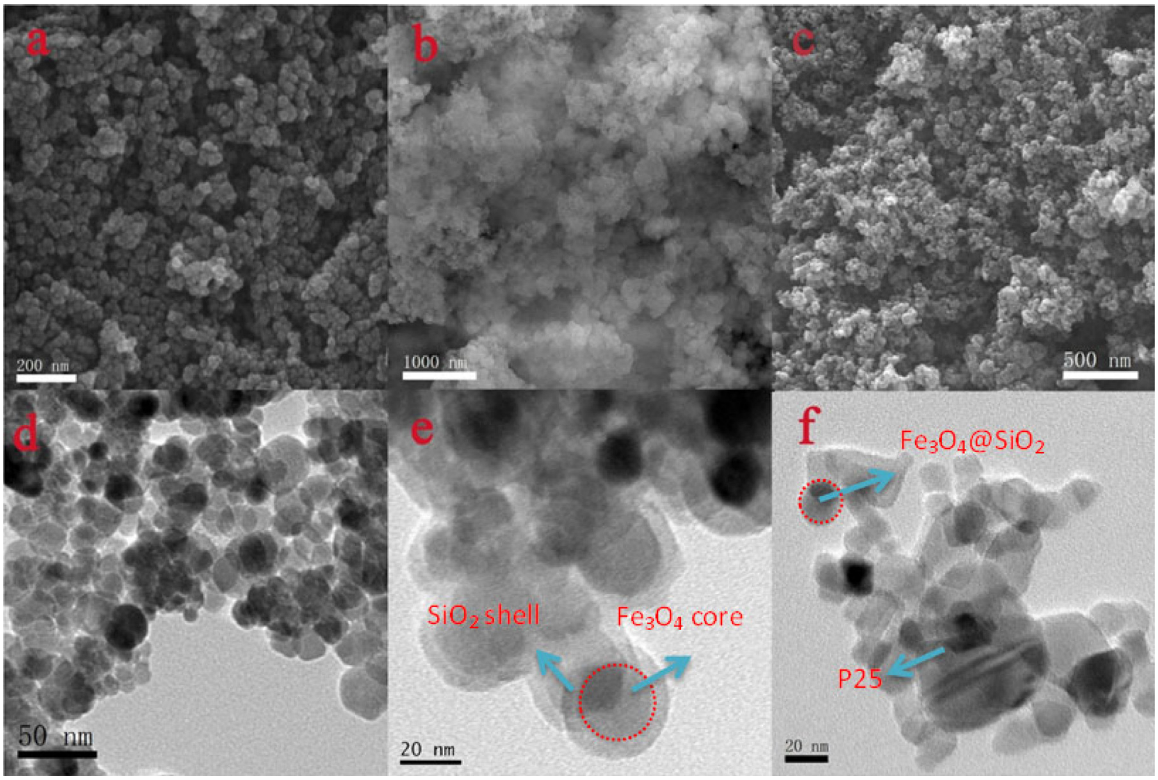

Fig. 2. SEM images of Fe_3O_4 (a), $Fe_3O_4@SiO_2$ (b), P25/$Fe_3O_4@SiO_2$ (c) and HR-TEM images of Fe_3O_4 (d), $Fe_3O_4@SiO_2$ (e), P25/$Fe_3O_4@SiO_2$ (f).

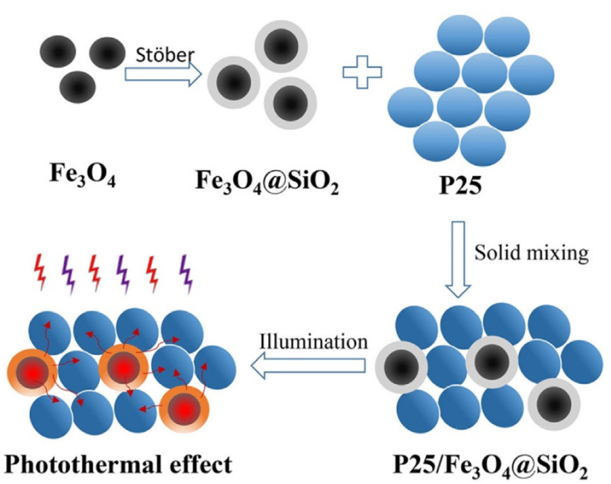

Fig. 3. The schematic diagrams of formation process of P25/$Fe_3O_4@SiO_2$ and the promotion process of photothermal effect.

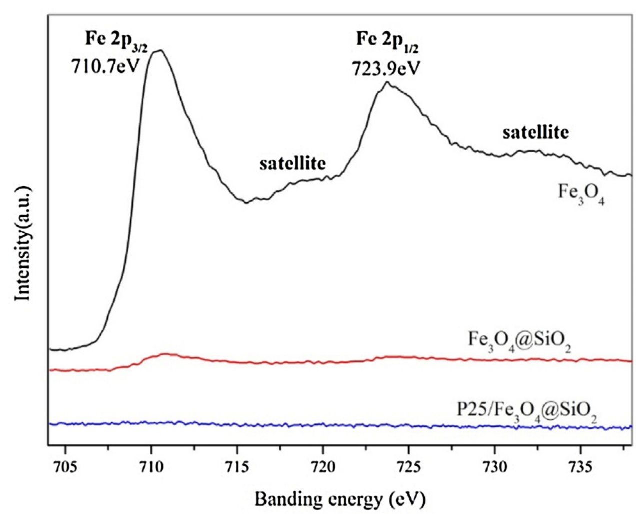

Fig. 4. Fe 2p spectra of Fe_3O_4, $Fe_3O_4@SiO_2$ and P25/$Fe_3O_4@SiO_2$.

3.3. Elemental analysis by XPS

X ray photoelectron spectroscopy (XPS) was used to determine the detailed elemental composition and oxidation state of the as-prepared samples, specially for the distribution of iron element. The Fe 2p spectra of Fe_3O_4, $Fe_3O_4@SiO_2$ and P25/$Fe_3O_4@SiO_2$(3:1) were shown in Fig. 4. Fe $2p_{3/2}$(710.7 eV), Fe $2p_{1/2}$(723.9 eV) and two satellite peaks of Fe_3O_4 were clearly demonstrated in the XPS spectrum of Fe_3O_4 [35], and this result correlated with the result of XRD spectrum. Furthermore, the characteristic peaks of Fe_3O_4 nearly disappeared in the XPS spectrum of $Fe_3O_4@SiO_2$ and disappeared in the XPS spectrum of P25/$Fe_3O_4@SiO_2$(3:1). The XPS results confirmed that Fe_3O_4 was well coated by SiO_2 with the core-shell structure of $Fe_3O_4@SiO_2$ [36]. The XPS spectra of Ti, O and Si elements are also presented in Fig. S2. The spectra demonstrated that Ti, O and Si elements coexisted in the as-prepared samples, and no peaks of any other elements were detected.

3.4. UV–vis-NIR light absorption

Fig. 5 shows the UV–vis-NIR light absorption spectra of prepared photocatalysts. Obviously, P25 exhibited a strong light absorption in UV light region and a very slight absorption in infrared region. However, Fe_3O_4 and $Fe_3O_4@SiO_2$ exhibited a strong absorption in the full light spectrum including the ultra violet light, the visible light and the infrared light region. After the coating of SiO_2 shell, the absorbance of $Fe_3O_4@SiO_2$ was weaker than that of Fe_3O_4. For the

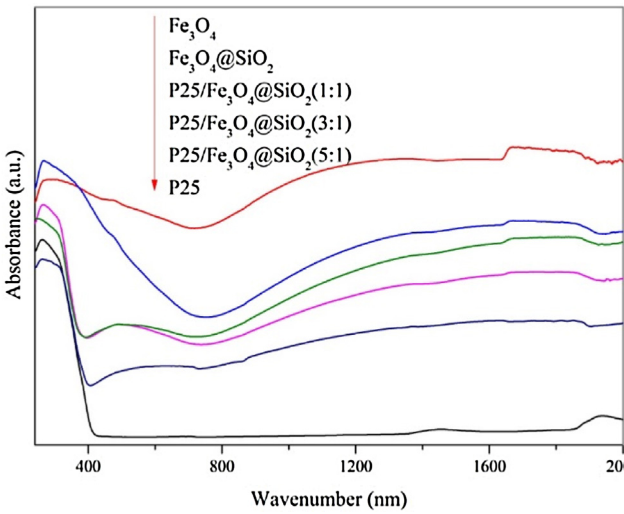

Fig. 5. UV–vis-NIR DRS spectra of photocatalysts.

mixture of P25 and Fe_3O_4@SiO_2 (P25/Fe_3O_4@SiO_2), the absorption strength fell in between P25 and Fe_3O_4@SiO_2, and covered the full spectrum too.

Otherwise, absorption strength of P25/Fe_3O_4@SiO_2 was enhanced with increased percentage of Fe_3O_4@SiO_2. The absorption in full light spectrum of P25/Fe_3O_4@SiO_2 made it possible to use solar energy of NIR light. Also, the UV–vis-NIR spectra of A TiO_2/Fe_3O_4@SiO_2, g-C_3N_4/Fe_3O_4@SiO_2, ZnO/Fe_3O_4@SiO_2, BiOI/Fe_3O_4@SiO_2 and CeO_2/Fe_3O_4@ SiO_2 were shown in Fig. S3. UV–vis-NIR spectra verified that the addition of Fe_3O_4 enhanced the NIR light absorption of prepared samples.

3.5. Thermo stability investigation

The antioxidation properties of SiO_2 shell was analyzed by TG curves of Fe_3O_4 and Fe_3O_4@SiO_2 in Fig. 6a as reported [37]. For Fe_3O_4, a little weight loss was observed when the temperature was lower than 122 °C, and then the loss mass began to increase at 122 °C and approached the maximum value at 211 °C due to the oxidation of Fe_3O_4. After the coating of SiO_2 shell, Fe_3O_4@SiO_2 showed a weight loss around 2% due to desorption of water and organic materials in the first stage (from 50 °C to 150 °C). After that, the mass of Fe_3O_4@SiO_2 showed little change in the calcination procedure. That meant the oxidation of Fe_3O_4 was inhibited by the core-shell structure of Fe_3O_4@SiO_2. The protection effect of SiO_2 can also be verified by comparison of Fe_3O_4 and Fe_3O_4@SiO_2 after photocatalytic reaction in Fig. 6b. For Fe_3O_4 and Fe_3O_4@SiO_2, the peaks at 355, 496 and 718 cm^{-1} were assigned to the E_g, T_{2g}, and A_{1g} modes of a typical magnetite Fe_3O_4 [38]. After the photocatalytic process, new peaks at 220, 286 and 405 cm^{-1} representing α-Fe_2O_3 appeared [39], confirming the oxidation of Fe_3O_4. However, no remarkable change was observed for Fe_3O_4@SiO_2 after the reaction. To further illustrate the protection of SiO_2, Fe 2p spectra of Fe_3O_4 and Fe_3O_4@SiO_2 treated at different temperatures for 2 h were shown in Fig. S4a and the comparison of samples after photocatalytic performance was shown in Fig. S4b. Obviously, the Fe 2p spectra of Fe_3O_4 after treated at 120 °C or after photocatalytic reaction exhibited shift compared to the Fe_3O_4, which may be attributed to the oxidation of Fe_3O_4. Relatively, the Fe 2p spectra of Fe_3O_4@SiO_2 remained unchanged after treated in hot circumstances or after the reaction.

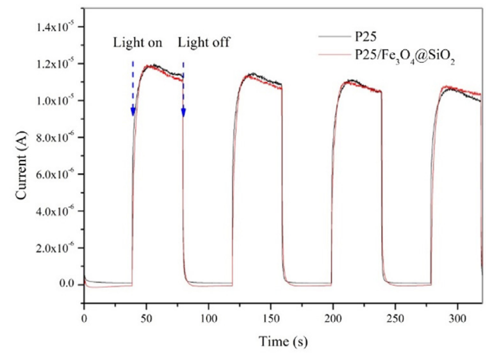

Fig. 7. Transient photocurrent responses of P25 and as-synthesized P25/Fe_3O_4@SiO_2 under the irradiation of UV–vis-NIR light.

3.6. Photoelectric current investigation

To better understand the promotion mechanism, photo-electric current experiments were carried out to investigate the photo-triggered charges density over P25 and P25/Fe_3O_4@SiO_2 under UV–vis-NIR light irradiation. As shown in Fig. 7, the photocurrent intensity of P25/Fe_3O_4@SiO_2 showed little change compared to P25 under the irradiation of UV–vis-NIR light. Thus it confirmed that

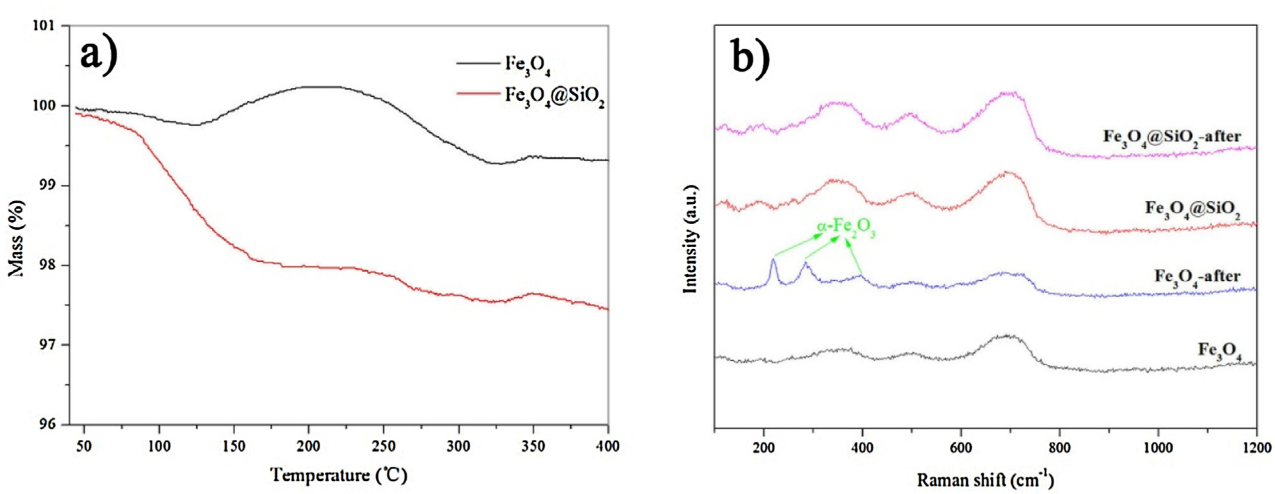

Fig. 6. TG curves of Fe_3O_4 and Fe_3O_4@SiO_2 (a) and Raman spectra of samples after photocatalytic reaction (b).

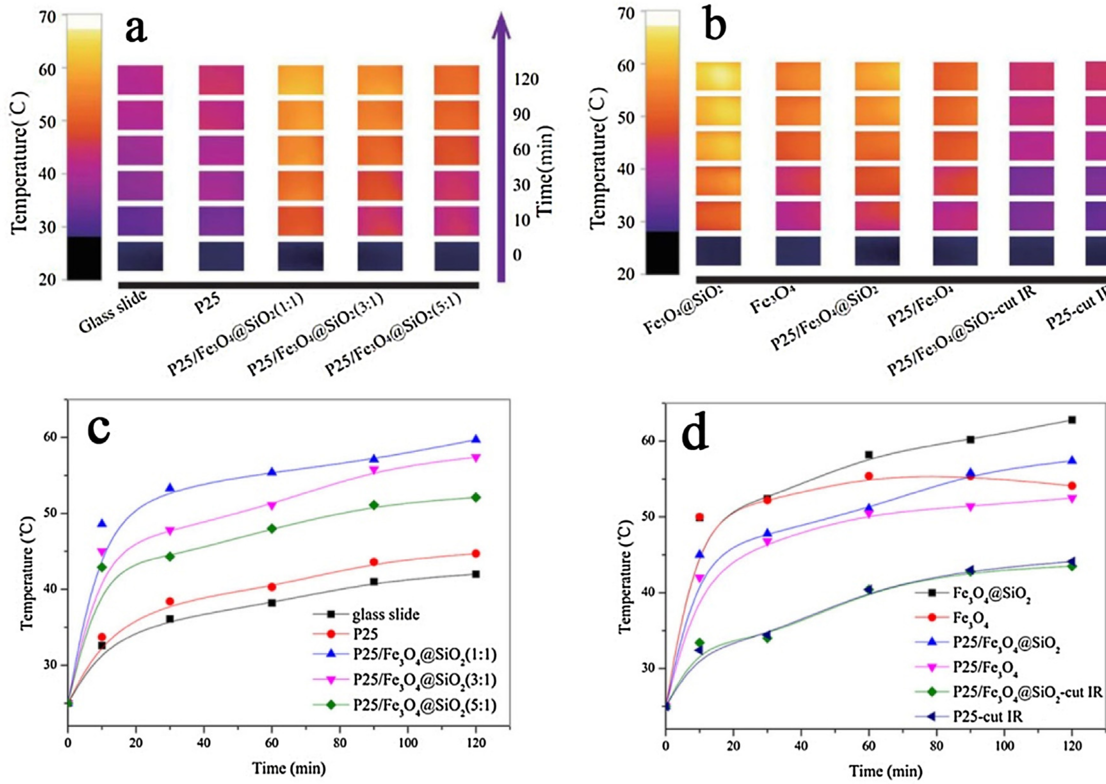

Fig. 8. Thermo images of samples (a) and (b), and photothermal effect of samples (c) and (d).

the photo-triggered charges density of P25 was not affected by the introduced $Fe_3O_4@SiO_2$.

3.7. IR thermo images

In this study, we used IR thermo images to measure the photothermal effect quantitatively by the surface temperature rise of samples obtained by the UV–vis-NIR irradiation via IR thermo images. The whole increment of thermal energy during photocatalytic reaction can be divided into two parts—directly thermal radiation from Xeon lamp and thermal energy generated by photothermal effect of plasmonic particles (if it existed in the system). In generally, the increment of thermal energy caused by directly thermal radiation can be regarded as a constant under the same irradiation condition. Thus it can be concluded there will be a positive contribution for the whole increment of thermal energy if the photothermal effect takes place in the system.

To take IR thermo images, experiments were carried out as follows. Samples were loaded on glass slide with the same method as photocatalytic experiments and placed in the channels of the reactor. The temperature of the reactor was controlled at 25 °C. IR thermo images were taken at 0, 10, 30, 60, 90 and 120 min after the Xeon lamp on. When taking the thermo images free from the irradiation of infrared light (P25-cut IR and P25/$Fe_3O_4@SiO_2$-cut IR), the infrared cut-off filter was used in the experiments.

The IR thermo images of samples were shown in Fig. 8a and b. The color of images was varied with the degree of temperature and the left scales corresponding to different color (Thermo images of “T” shape Fe_3O_4 in the center of P25 were shown in Fig. S5). With the irradiation of UV–vis-NIR light, temperature of every sample rose with the increase of irradiation time. The color of images of P25/$Fe_3O_4@SiO_2$ became brighter, when more $Fe_3O_4@SiO_2$ NPs were added (Fig. 8a). However, the color of the image of P25 showed inconspicuous change with a 120 min light irradiation, same as that of blank glass slide. The specific temperature data (Fig. 8c) was also obtained to present the photothermal effect accurately. The temperature of blank glass slide (Fig. 8c) with no sample rose gradually from 25 °C to 42 °C after illumination for 120 min. Compared to glass slide, the temperature of the surface of P25 (Fig. 8c) rose a little more to 44.7 °C, indicating that P25 exhibited a slight photothermal effect contributed by the combination of hole and electron during the UV light irradiation. When $Fe_3O_4@SiO_2$ was mixed with P25 (Fig. 8c), the temperature of photocatalysts rose obviously. The surface temperature of P25/$Fe_3O_4@SiO_2$(1:1), P25/$Fe_3O_4@SiO_2$(3:1) and P25/$Fe_3O_4@SiO_2$(5:1) increased form 25 °C to 59.7 °C, 57.4 °C and 52.1 °C, respectively. With the increase of $Fe_3O_4@SiO_2$, the rise of temperature became more evident. From above findings, we can conclude that the increment of thermal energy was mainly attributed to the photothermal effect of $Fe_3O_4@SiO_2$ and depended on the content of $Fe_3O_4@SiO_2$.

The protection effect of SiO_2 shell to Fe_3O_4 NPs and the influence of infrared light were analyzed in Fig. 8d. It was found that temperature rise of Fe_3O_4 NPs was higher than that of $Fe_3O_4@SiO_2$ NPs in the first 30 min. However, the increment of temperature became weaker in the followed irradiation time and even appeared a decline trend. For the comparison of P25/Fe_3O_4 and P25/$Fe_3O_4@SiO_2$, P25/$Fe_3O_4@SiO_2$ got a higher increment of temperature during the whole illumination time and the variation trend of temperature of P25/Fe_3O_4 was similar to that of Fe_3O_4. Based on the analysis of the four samples, the photothermal effect of Fe_3O_4 and P25/Fe_3O_4 was weakened with increased irradiation time and increased surface temperature. However, $Fe_3O_4@SiO_2$ and P25/$Fe_3O_4@SiO_2$ maintained the photothermal effect during the entire experiment. After reaction, photothermal effect of Fe_3O_4 disappeared while photothermal effect of $Fe_3O_4@SiO_2$ maintained in Fig. S6. Combining the result of TG and Raman (Fig. 5), it could be concluded that Fe_3O_4 NPs was oxidized by products from photocatalytic reaction or oxygen under this hot circumstance and

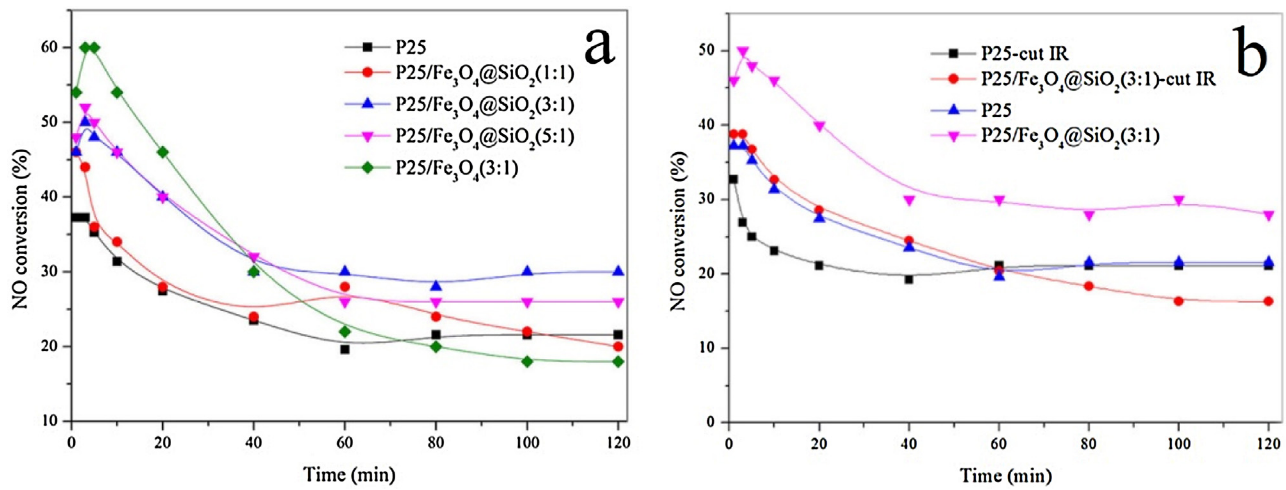

Fig. 9. Photocatalytic oxidation of NO of samples (a) and the impact of NIR on NO conversion (b).

its photothermal effect was destroyed. Nevertheless, $Fe_3O_4@SiO_2$ NPs maintained its photothermal effect because of the protection of SiO_2. In addition, the temperature curves of P25-cut IR and $P25/Fe_3O_4@SiO_2$-cut IR (Fig. 7d) nearly overlap with the cutting of infrared light, which demonstrated that infrared light was indispensable for photothermal effect of $Fe_3O_4@SiO_2$.

3.8. Photocatalytic oxidation of NO and proposed promotion mechanism

The NO conversion of the prepared samples was shown in Fig. 9. In the experiments, pure Fe_3O_4 and $Fe_3O_4@SiO_2$ had no capacity to convert NO under the irradiation of UV–vis-NIR light. As shown in Fig. 9a, NO conversion of P25 was 21.6% in steady condition. Obviously, the photocatalytic activity of $P25/Fe_3O_4@SiO_2$ was changed with the addition of $Fe_3O_4@SiO_2$. With the increasing ratio of $Fe_3O_4@SiO_2$, NO conversion increased at first then decreased and the optimal mass ratio of P25 and $Fe_3O_4@SiO_2$ was 3:1. For $P25/Fe_3O_4@SiO_2$(3:1), the NO conversion achieved 30% and an activity enhancement of 38.9% was achieved. It could be deduced that an excess of $Fe_3O_4@SiO_2$ would occupy the irradiation surface of photocatalysts and result in insufficient P25 with photocatalytic activity for the reaction on the surface. Whereas the lack of $Fe_3O_4@SiO_2$ could not realize the effective usage of thermal energy generated from photothermal effect. Reasonably, an optimized $P25/Fe_3O_4@SiO_2$(3:1) was obtained with proper amount of P25 and $Fe_3O_4@SiO_2$ to provide active species and photothermal effect. The influence of the introduction of $Fe_3O_4@SiO_2$ on the selectivity of photocatalytic products was investigated. In the initial of the photocatalytic process, HNO_3 and NO_2 were the main products for both P25 and $P25/Fe_3O_4@SiO_2$ [40], and the NO_3^- coated on the photocatalyst could be detected in the in-situ FTIR spectra in Fig. S7 (peaks at 1538, 1419, 1330 and 1290 cm^{-1}) [41–43]. With the reaction time increased, NO_2 gradually became the only product, which could be verified by the NO_2 selectivity of the composed samples in Fig. S8. After 40 min, the NO_2 selectivity for every photocatalyst reached 100%, which indicated that the introduction of $Fe_3O_4@SiO_2$ had no influence on the selectivity of products during photocatalytic process.

To confirm the protection effect of SiO_2 shell, the photocatalytic activity of $P25/Fe_3O_4$(3:1) was also measured in the experiment. With the irradiation of UV–vis-NIR light, $P25/Fe_3O_4$(3:1) exhibited higher photocatalytic activity compared to P25 in the first 40 min. But its photocatalytic activity decreased gradually with the progress of reaction and even got an 18% NO conversion in the end of experiment, which was lower than that of pure P25. Evidently, the enhancement of photocatalytic activity in the first 40 min was attributed to the photothermal effect of Fe_3O_4 and this effect disappeared with the oxidation or corrosion of Fe_3O_4. For the description of promotion effect, the influence of infrared light on photocatalytic activity was shown in Fig. 9b. When an infrared light cut-off filter placed on the quarts, the NO conversion of P25 (P25-cut IR) decreased slightly. However, the NO conversion of $P25/Fe_3O_4@SiO_2$(3:1) ($P25/Fe_3O_4@SiO_2$(3:1)-cut IR) decreased to 16%. Besides, after experiment conducted, $P25/Fe_3O_4@SiO_2$ exhibited no photocatalytic activity under NIR light irradiation. Therefore, it could be concluded that the irradiation of NIR light was the control factor for the promotion of photocatalytic activity of $P25/Fe_3O_4@SiO_2$.

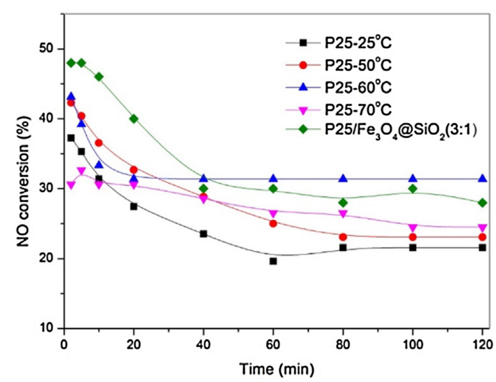

Fig. 10. Photocatalytic oxidation of NO by P25 under different reaction temperatures.

In order to verify the promotion mechanism led by the photothermal effect, the photocatalytic oxidation of NO under different reaction temperatures were conducted in Fig. 10. With the rise of reaction temperature, NO conversion of P25 increased at first and then decreased in the followed procedure and the optimal reaction temperature reached at 60 °C. The increase of temperature would increase the ratio of activated molecules and then enhance the photocatalytic activity of NO. However, the increase of temperature was in favor of desorption of NO. Thus it is not difficult to understand that an optimum reaction temperature around 60 °C was obtained due to the balance between molecule activation and desorption of NO. Based on the photocurrent intensity analysis of $P25/Fe_3O_4@SiO_2$ and P25 (Fig. 7), we figured that the hot electrons excited by plasmonic nanocrystals didn't transfer to the

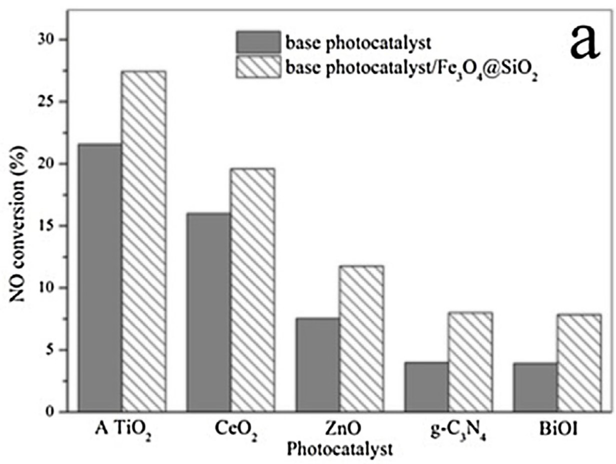

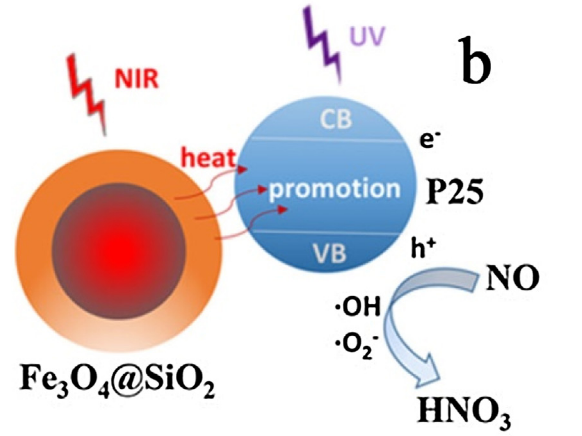

Fig. 11. Promotion of photocatalytic activity for different photocatalysts (a) and promotion mechanism of the photothermal effect based on infrared light for photocatalytic reaction (b).

antibonding orbitals of P25. Thus, P25/Fe_3O_4@SiO_2(3:1) obtained NO conversion close to that of P25 under 60 °C, which could be attributed to the approximate temperature (Shown in Fig. 8c) caused by the photothermal effect.

To verify the promotion mechanism of photothermal effect led by Fe_3O_4@SiO_2, the photocatalytic activity of NO of five kinds of typical photocatalysts mixed with Fe_3O_4@SiO_2 were also measured in the study (Fig. 11a). It was worth mentioning that the activity of A TiO_2/Fe_3O_4@SiO_2, g-C_3N_4/Fe_3O_4@SiO_2, ZnO/CeO_2/Fe_3O_4@SiO_2, BiOI/Fe_3O_4@SiO_2 and CeO_2/Fe_3O_4@SiO_2 were all enhanced by the addition of Fe_3O_4@SiO_2. Evidently, an increment of NO conversion capability around 30–40% was observed for the Fe_3O_4@SiO_2 mixed A TiO_2, g-C_3N_4, ZnO, BiOI and CeO_2. Finally, the promotion mechanism of photothermal effect based on infrared light for photocatalysis reaction was proposed and shown in Fig. 11b.

4. Conclusion

In conclusion, photothermal effect was first utilized in this study to capture the energy of infrared light and promoted the photocatalytic oxidation capability of NO simply by mixing base photocatalyst—P25 and core-shell structured Fe_3O_4@SiO_2. Fe_3O_4@SiO_2 absorbed the infrared light, transferred it to thermal energy based on photothermal effect, and then accelerated the NO photocatalytic activity of base photocatalysts.

The addition of Fe_3O_4@SiO_2 enhanced the NIR light absorption of P25/Fe_3O_4@SiO_2 in UV–vis-NIR spectrum. But, the photocurrent intensity of P25/Fe_3O_4@SiO_2 showed little change with comparison to pure P25 under the irradiation of UV–vis-NIR light. And it confirmed that the photo-triggered charges density of P25 was not affected by the introduced Fe_3O_4@SiO_2. With the protection of the SiO_2 shell, oxidation of Fe_3O_4 was inhibited during the photocatalytic procedure. When Fe_3O_4@SiO_2 was mixed with P25, the temperature of P25/Fe_3O_4@SiO_2 rose obviously and the rise of temperature showed a positive relation with the percentage of Fe_3O_4@SiO_2. The amount of Fe_3O_4@SiO_2 was a vital factor for the promotion of photocatalytic activity and the optimum mass ratio of P25 and Fe_3O_4@SiO_2 was 3–1. Under the optimum mass ratio of P25 and Fe_3O_4@SiO_2, an activity enhancement of 38.9% was reached compared to pure P25. The photocatalytic experiments under different reaction temperature verified that the contribution of photothermal effect was same as the directly heating of photocatalysts. Furthermore, the enhancement of NO conversion capability around 30–40% was observed for the Fe_3O_4@SiO_2 mixed A TiO_2, g-C_3N_4, ZnO, BiOI and CeO_2. We hope this new strategy for the utilization of NIR light of solar energy could inspire more advanced and sophisticated catalyst designed with rational ideas aiming at the usage of solar energy.

Acknowledgments

This research is financially supported by National Natural Science Foundation of China (NSFC-51578488), Special Program for Social Development of Key Science and Technology Project of Zhejiang Province (2014C03025), Zhejiang Provincial "151" Talents Program, and the Program for Zhejiang Leading Team of S&T Innovation (Grant No. 2013TD07).

Appendix A. Supplementary data

Supplementary data associated with this article can be found, in the online version, at http://dx.doi.org/10.1016/j.apcatb.2016.12.009.

References

[1] G. Ou, Z.W. Li, D.K. Li, L. Cheng, Z. Liu, H. Wu, Nano Res. 9 (2016) 1236–1243.
[2] E.S. Elmolla, M. Chaudhuri, Desalination 252 (2010) 46–52.
[3] J. Andersen, C. Han, K. O'Shea, D.D. Dionysiou, Appl. Catal. B: Environ. 154 (2014) 259–266.
[4] S.C. Yan, Z.S. Li, Z.G. Zou, Langmuir 26 (2010) 3894–3901.
[5] Y. Huang, W. Wang, Q. Zhang, J.J. Cao, R.J. Huang, W.K. Ho, S.C. Lee, Sci. Rep. 6 (2016).
[6] M. Li, H.W. Huang, S.X. Yu, N. Tian, F. Dong, X. Du, Y.H. Zhang, Appl. Surf. Sci. 386 (2016) 285–295.
[7] W. Qin, D. Zhang, D. Zhao, L. Wang, K. Zheng, Chem. Commun. 46 (2010) 2304–2306.
[8] M. Mao, Y. Li, J. Hou, M. Zeng, X. Zhao, Appl. Catal. B: Environ. 174–175 (2015) 496–503.
[9] K. Yang, L.Z. Feng, X.Z. Shi, Z. Liu, Chem. Soc. Rev. 42 (2013) 530–547.
[10] Q.W. Tian, M.H. Tang, Y.G. Sun, R.J. Zou, Z.G. Chen, M.F. Zhu, S.P. Yang, J.L. Wang, J.H. Wang, J.Q. Hu, Adv. Mater. 23 (2011) 3542–3547.
[11] G. Shafirstein, W. Baumler, L.J. Hennings, E.R. Siegel, R. Friedman, M.A. Moreno, J. Webber, C. Jackson, R.J. Griffin, Int. J. Cancer 130 (2012) 1208–1215.
[12] J. Yang, J. Choi, D. Bang, E. Kim, E.K. Lim, H. Park, J.S. Suh, K. Lee, K.H. Yoo, E.K. Kim, Y.M. Huh, S. Haam, Angew. Chem. Int. Ed. 50 (2011) 441–444.
[13] H. Zakaria, W.S. Abdelaziz, T. Youssef, Lasers Med. Sci. 31 (2016) 625–634.
[14] J.J. Shi, L. Wang, J. Zhang, R. Ma, J. Gao, Y. Liu, C.F. Zhang, Z.Z. Zhang, Biomaterials 35 (2014) 5847–5861.
[15] W.J. Fang, S.H. Tang, P.X. Liu, X.L. Fang, J.W. Gong, N.F. Zheng, Small 8 (2012) 3816–3822.
[16] L. Wang, J.J. Shi, H.L. Zhang, H.X. Li, Y. Gao, Z.Z. Wang, H.H. Wang, L.L. Li, C.F. Zhang, C.Q. Chen, Z.Z. Zhang, Y. Zhang, Biomaterials 34 (2013) 262–274.
[17] O. Akhavan, E. Ghaderi, Small 9 (2013) 3593–3601.

[18] P. Kalluru, R. Vankayala, C.S. Chiang, K.C. Hwang, Biomaterials 95 (2016) 1–10.
[19] M.Q. Chu, Y.X. Shao, J.L. Peng, X.Y. Dai, H.K. Li, Q.S. Wu, D.L. Shi, Biomaterials 34 (2013) 4078–4088.
[20] J. Chen, Z. Guo, H.B. Wang, M. Gong, X.K. Kong, P. Xia, Q.W. Chen, Biomaterials 34 (2013) 571–581.
[21] P. An, F. Zuo, X.H. Li, Y.P. Wu, J.H. Zhang, Z.H. Zheng, X.B. Ding, Y.X. Peng, Nano 8 (2013).
[22] J. Liu, P.Y. Wang, X. Zhang, L.M. Wang, D.L. Wang, Z.J. Gu, J.L. Tang, M.Y. Guo, M.J. Cao, H.G. Zhou, Y. Liu, C.Y. Chen, ACS Nano 10 (2016) 4587–4598.
[23] Q.W. Tian, F.R. Jiang, R.J. Zou, Q. Liu, Z.G. Chen, M.F. Zhu, S.P. Yang, J.L. Wang, J.H. Wang, J.Q. Hu, ACS Nano 5 (2011) 9761–9771.
[24] R.J.G. Johnson, K.M. Haas, B.J. Lear, Chem. Commun. 51 (2015) 417–420.
[25] Z.X. Gan, X.L. Wu, M. Meng, X.B. Zhu, L. Yang, P.K. Chu, ACS Nano 8 (2014) 9304–9310.
[26] Y.N. Tang, W.H. Di, X.S. Zhai, R.Y. Yang, W.P. Qin, ACS Catal. 3 (2013) 405–412.
[27] S.I. Nikitenko, T. Chave, C. Cau, H.P. Brau, V. Flaud, ACS Catal. 5 (2015) 4790–4795.
[28] P. Dong, N. Xu, Y. Xu, X. Wang, Catal. Commun. 84 (2016) 142–146.
[29] Y. Wang, S. Zhang, Y. Zeng, M. Ou, Q. Zhong, J. Mol. Catal. A: Chem. 423 (2016) 339–346.
[30] S. Cao, H.Q. Wang, F.X. Yu, M.P. Shi, S. Chen, X.L. Weng, Y. Liu, Z.B.A. Wu, J. Colloid Interface Sci. 463 (2016) 233–241.
[31] F. Dong, L.W. Wu, Y.J. Sun, M. Fu, Z.B. Wu, S.C. Lee, J. Mater. Chem. 21 (2011) 15171–15174.
[32] K. Buvaneswari, R. Karthiga, B. Kavitha, M. Rajarajan, A. Suganthi, Appl. Surf. Sci. 356 (2015) 333–340.
[33] J. Cao, C.C. Zhou, H.L. Lin, B.Y. Xu, S.F. Chen, Mater. Lett. 109 (2013) 74–77.
[34] X.J. Liang, W.W. Huan, X.C. Jia, H.J. Ding, Y.X. Yang, X.N. Liu, Nano 5 (2010) 203–214.
[35] R.J. Wang, X.Y. Liu, R.H. Wu, B.W. Yu, H.L. Li, X.L. Zhang, J.R. Xie, S.T. Yang, RSC Adv. 6 (2016) 8594–8600.
[36] J.S. Choi, H.K. Youn, B.H. Kwak, Q. Wang, K.S. Yang, J.S. Chung, Appl. Catal. B: Environ. 91 (2009) 210–216.
[37] Y.H. Leng, K. Sato, Y.G. Shi, J.G. Li, T. Ishigaki, T. Yoshida, H. Kamiya, J. Phys. Chem. C 113 (2009) 16681–16685.
[38] F. Jiang, X. Wang, D. Wu, Appl. Energy 134 (2014) 456–468.
[39] V.I. Al'myashev, K.G. Gareev, S.A. Ionin, V.S. Levitskii, V.A. Moshnikov, E.I. Terukov, Phys. Solid State 56 (2014) 2155–2159.
[40] S. Devahasdin, C. Fan, K.Y. Li, D.H. Chen, J. Photochem. Photobiol. A: Chem. 156 (2003) 161–170.
[41] L. Sivachandiran, F. Thevenet, A. Rousseau, D. Bianchi, Appl. Catal. B: Environ. 198 (2016) 411–419.
[42] R.V. Mikhaylov, A.A. Lisachenko, B.N. Shelimov, V.B. Kazansky, G. Martra, S. Coluccia, J. Phys. Chem. C 117 (2013) 10345–10352.
[43] K. Hashimoto, K. Wasada, M. Osaki, E. Shono, K. Adachi, N. Toukai, H. Kominami, Y. Kera, Appl. Catal. B: Environ. 30 (2001) 429–436.